China Steel Technical Report, No. 32, pp.44 −54, (2019)

Influence of Particle Size on Microstructural and Magnetic Properties of Yttrium Iron Garnet Ferrite

HING-CHIEN HUANG*, JING-YI HUANG, WEI-ZONG ZUO**, CHEN-FENG CHAN*, CHIH-CHIEH MO** and MING-FENG KUO***

** New Materials Research & Development Department, China Steel Corporation*
*** Himag Magnetic Corporation*

Yttrium iron garnet ferrite using the chosen stoichiometry of $(Y_3)(Mn_xAl_{0.8-x}Fe_{4.2})O_{12}$ with $x = 0.1$ and different milling powder sizes were prepared through ball milling for various milling times to study the effect of powder size reduction on the resulting microstructural and magnetic properties. Sintered yttrium iron garnet ferrites were characterized by X-ray diffraction analysis and scanning electron microscopy. The particle size (D_{50}) of as-milled calcined powder was decreased using ball milling (from 3.682 μm for a 0.5-h-long milling to 1.606 μm for a 2.5-h-long milling). Scanning electron microscopy analyses confirmed that the sintered grain exhibited a crystal size that was increased from initial values (average crystal grain sizes of 3.5 ± 0.1μm for 0.5h of milling) up to 6.2 ± 0.1μm after 2.5 h of ball milling and the subsequent sintering process. The same sintered specimen after 2.5 h of ball milling exhibited an obvious increase in saturation magnetization ($4\pi M_s$), remanence (B_r), and squareness ratio (namely $B_r/4\pi M_s$); it also caused a notable decline in coercivity (H_c) and ferromagnetic resonance line width (ΔH), which were attributed to the introduction of a smaller size of calcined powder after milling and subsequently resulted in a larger sintered grain. Furthermore, a sufficient spin-wave line width (ΔH_k) and low insertion loss ($|S_{21}|$) were obtained for the operation of the microwave device. The aforementioned results are all beneficial to the use of yttrium iron garnet ferrite in microwave applications. A correlation between the calcined powder size after milling, grain crystal size after sintering, and magnetic properties was evident in this study. The strict control of calcined powder size after milling is critical in tailoring suitable magnetic properties for yttrium iron garnet ferrite manufacturing processes.

Keywords: Ball Mill, Calcined Powder, Coercivity (H_c), Ferromagnetic Resonance Line Width (ΔH), Insertion Loss ($|S_{21}|$), Particle Size, Remanence (B_r), Saturation Magnetization ($4\pi M_s$), Spin-wave Line Width (ΔH_k), Squareness Ratio (SQR), Yttrium Iron Garnet (YIG) Ferrite.

1. INTRODUCTION

Yttrium iron garnet (YIG) is a ferrite material with excellent magnetic properties, making it a promising candidate for use in high performance microwave and electrochemical devices, such as circulators and latching-type phase shifters. This is due to its high resistivity, Curie temperature (T_c), and chemical stability, in addition to its thermophysical, mechanical, and unique magnetic properties such as narrow ferromagnetic resonance (FMR) line width (ΔH), and low dielectric loss[1-6]. YIG possesses a cubic crystal structure with a general formula of $A_3B_5O_{12}$ and specific formula of $Y_3Fe_5O_{12}$. The unit cell of YIG comprises eight formula units forming a complex cubic lattice constituted by 160 ions in specific lattice positions. Three sublattices are present in the garnet structure; the dodecahedra *c*-site is occupied by three Y^{3+}, the octahedral *a*-site is occupied by two Fe^{3+}, and the tetrahedral *d*-site is occupied three Fe^{3+}. The Y^{3+} and Fe^{3+} present in the sites are trivalent, making YIG exceptionally suitable for magnetic studies[7, 8]. Notably, the magnetic moment of Yttrium is insensitive to the crystalline field, and the super-exchange anisotropy is zero due to the absence of net orbital angular momentum (usually denoted as *L*). The dominating super-exchange interaction renders the magnetic moments of the *a*-site and *d*-site antiparallel aligned, and determines the T_C. Whereas the magnetic moments of two Fe^{3+} from the *d*-site are canceled out by that of the two Fe^{3+} from the *a*-site, the resultant magnetization of the Fe^{3+} sublattices is opposite to the magnetization of Y^{3+}, giving rise to ferrimagnetism. Thus, the magnetic moment of YIG is a result of the surplus Fe^{3+} from the *d*-site.

YIG ferrites are often used in microwave phase shifters for scanning radar beams[9]. To effectively control the microwave properties for the devices applied, the characteristics or the shape of the hysteresis loop and the magnetic properties are critical[7]. However, the need for a phase shifter that can be switched in a few microseconds has placed a new emphasis on ferrite. Fast

switching characteristics for phase shifters cannot be obtained without a low coercivity (H_c), such as from the hysteresis properties of ferrite[12]. In addition, square hysteresis loops for ferrite are arranged in closed magnetic paths. The two remanent states of magnetization corresponding to the two stable states are critical to the phase shifter. A higher squareness ratio (*SQR*) (i.e., $B_r/4\pi M_s$) leads to superior switching of the phase shifter[12]. The bistatic characteristics of the phase shifter render it an attractive component for application in phase-array radar systems[12]. For our study, the hysteresis characteristics of ferrite (e.g., $4\pi M_s$, approximately 650 Gauss, $H_c < 1.0$ Oe, $SQR > 0.85$) are required for S-band phase shifter applications[1, 7, 11, 12].

Material composition is essential to the properties of garnet ferrite, because the chosen stoichiometry forcefully determines the magnetic properties of YIG ferrite [8, 10]. Mn, Al-substituted YIG, which possesses a narrow ΔH with a low H_c at a relatively sufficient saturation magnetization ($4\pi M_s$) and *SQR* could be employed for latching-type phase shifters at S-band frequency ranges (3–5 GHz)[4, 11]. By substituting Mn and Al, the interaction between the sublattices of the YIG structure leads to a modification of their properties. As a result, reducing $4\pi M_s$ is desirable to achieve the required S-band phase shifter through Al substitution, while maintaining high *SQR*. However, an effort to obtain the required $4\pi M_s$ results in sacrificing *SQR*. We dealt with the property modification of high *SQR* through Mn substitution; that is, by increasing Mn^{x+} content. Replacing part of the proportion of Al with Mn was performed to maintain the value of B_r, while simultaneously achieving the required $4\pi M_s$.

YIG has a complex structure; thus, obtaining a single-phase YIG to achieve high magnetic properties is challenging. Not only are the intrinsic properties of YIG (composition of the material) notably relative to it magnetic properties, so too are the extrinsic properties (for example, the microstructure of polycrystalline YIG after sintering). Many properties of ferrites are related to their microstructures. However, other than stoichiometry and reaction temperature, the particle size of ferrite powder before the sintering process is also crucial in the reaction formation. Few studies have discussed the effect of the particle size of ferrite powder used for pressing and sintering. Most reactions during the sintering process, which transforms a powder into a solid body using heat, depend on particle collision; thus, the smaller the average particle size evaluated by the respective median diameters D_{50} (i.e., a larger specific surface area), the faster and more complete the reaction. A ball milling process is a solid-state technique used to prepare garnet ferrite[13, 14]. The effect of morphological changes on the polycrystalline YIG and ameliorating magnetic properties have not yet been experimentally established for microstructure evolution after sintering with finer-sized as-milled calcined powders yielded by a ball mill. By prolonging the ball milling time of calcined powders, a reduced particle size and narrowed-down particle size distribution can be produced, which are favorable for obtaining sufficient $4\pi M_s$, *SQR*, spin-wave line width (ΔH_k), as well as low H_c, ferromagnetic resonance line width (ΔH), and insertion loss ($|S_{21}|$).

The purpose of this study is to track the grain size evolution of sintering polycrystalline YIG with the dependence of particle size of calcined powder after different ball milling times, and to determine its attendant effects on magnetic properties ($4\pi M_s$, B_r, *SQR*, H_c, ΔH, ΔH_k, $|S_{21}|$). Studies have rarely illustrated this type of microstructure–property relationship.

2. EXPERIMENTAL METHOD

Mn and Al-doped particles were synthesized in polycrystalline form using a solid-state reaction technique to form a mixture of raw materials (i.e., α-Fe_2O_3 [China Steel Corporation (CSC)], iron oxide ≥ 99.99%; silicon oxide ≤ 0.015 wt%; calcium oxide ≤ 0.007 wt%), Y_2O_3 (99.99%), Mn_3O_4 (99.99%), and Al_2O_3 (99.99%). The raw materials were weighed with an accuracy of 0.0001g according to the chosen stoichiometry of (Y_3) $(Mn_xAl_{0.8-x}Fe_{4.2})$ O_{12} with $x = 0.1$ to achieve favorable magnetic properties[10] and then mixed in a ball mill for 3 h with alcohol and 3 kg of ZrO_2 balls to ensure the slurry could be mixed uniformly. The slurry was dried and then calcined at 1200°C for 2 h in an air atmosphere with a heating rate of 5°C/min. The calcined powders were remilled using a ball mill for five different corresponding milling times: (1) Sample A (ball milling time = 0.5 h); (2) Sample B (ball milling time = 1.0 h); (3) Sample C (ball milling time = 1.5 h); (4) Sample D (ball milling time = 2.0 h); (5) Sample E (ball milling time = 2.5 h). The obtained average particle sizes ranged from approximately 3.682 μm for 0.5 h of milling to 1.606 μm for 2.5 h of milling. After being milled, the calcined powders were pressed into cylindrical molds. Cold isostatic pressing at 200 MPa was used to improve the uniformity and density of the green bodies. The cold isostatic-pressed green compact density was approximately 2.8 g/cm^3. Next, the green bodies were sintered at 1400°C for 6 h in an air atmosphere with a heating rate of 5°C/min and furnace-cooled to room temperature. The densities of the sintered samples were then measured using the Archimedes method. The theoretical density was taken to be 5.17 g/cm^3 as suggested by Chou *et al.*[15]. Finally, the sintered bodies were mechanically processed into rectangular toroids, rods, and pellets with specific sizes to measure the magnetic characteristics of the ferrites according to IEC60556[16]. The specific size samples were polished before testing.

The hysteresis loop characteristics ($4\pi M_s$, B_r, H_c,

SQR) of the toroidal samples that were 10 turns wound were measured using a Yokogawa SK-130 *B-H* tracer analyzer graph at room temperature under applied magnetic fields of 0–50 Oe. The relative dielectric constant (ε_r) and loss (tanδ) were detected using the modified Hakki and Coleman approach[17, 18] in the TE_{011} mode using a network analyzer (Agilent E5071B) at a frequency range of 2–4 GHz. The microstructures of the sintered specimens were investigated using scanning electron microscopy (SEM). The crystalline structures of the ferrites were confirmed using an X-ray powder diffraction (XRD) technique. A crucial parameter of microwave magnetic material concerning magnetic losses, ΔH, was also measured in accordance with ASTM A883/A883M-01. For YIG ferrite applied in microwave devices above a certain microwave power level, another vital parameter concerning the corresponding power handling capability, ΔH_k, was measured using the cavity method. This is a traditional method for measuring the ΔH_k of YIG using a high-power microwave source with an adjustable frequency, and a rectangular cavity with a fixed frequency.

3. RESULTS AND DISCUSSION

3.1 Microstructure Analysis

The calcined powder microstructures of Samples A–E after different ball milling times are presented in Fig.1(a)–(e). The SEM micrographs were taken at random with 5000X magnification. Fig.1 reveals that a larger proportion of calcined powder after the longer ball milling time consisted of fewer multigrain particles. These images explain the discrepancy between the calculated and measured average particle size value, that is, the respective median diameters D_{50}; the longer the ball milling time, the fewer the multigrain particles, and consequently, the larger the corresponding specific surface area (SSA). Compared with the milled powder of Samples A, B, and C, the multigrain particles were larger and more uneven in Samples D and E. The morphology of the as-milled particles was small and even in size after longer ball milling times, which suggest favorability for ceramic processing. Fig.2 shows the comparison of particle size distribution of calcined powder in Samples A–E after different ball milling times. The data of average particle size (D_{50}) of the calcined powders after different ball milling times is shown in Fig.3. The smallest average particle size, D_{50}, is obtained when applying a longer ball milling time. The average particle size was measured using a SYMPATEC laser scattering system with a dry dispersion unit (System Rodos). Particle size distributions have been traditionally calculated based on sieve analysis results by creating an S-curve of cumulative mass retained against sieve mesh size and calculating the intercepts for 10%, 50%, and 90% mass. The D_{50} was used in this study to represent the midpoint and range of the average particle sizes of a given sample. Notably, larger SSAs of calcined powder after ball milling exhibit superior reactions in subsequent sintering processes. In addition to particle size, a narrow particle size

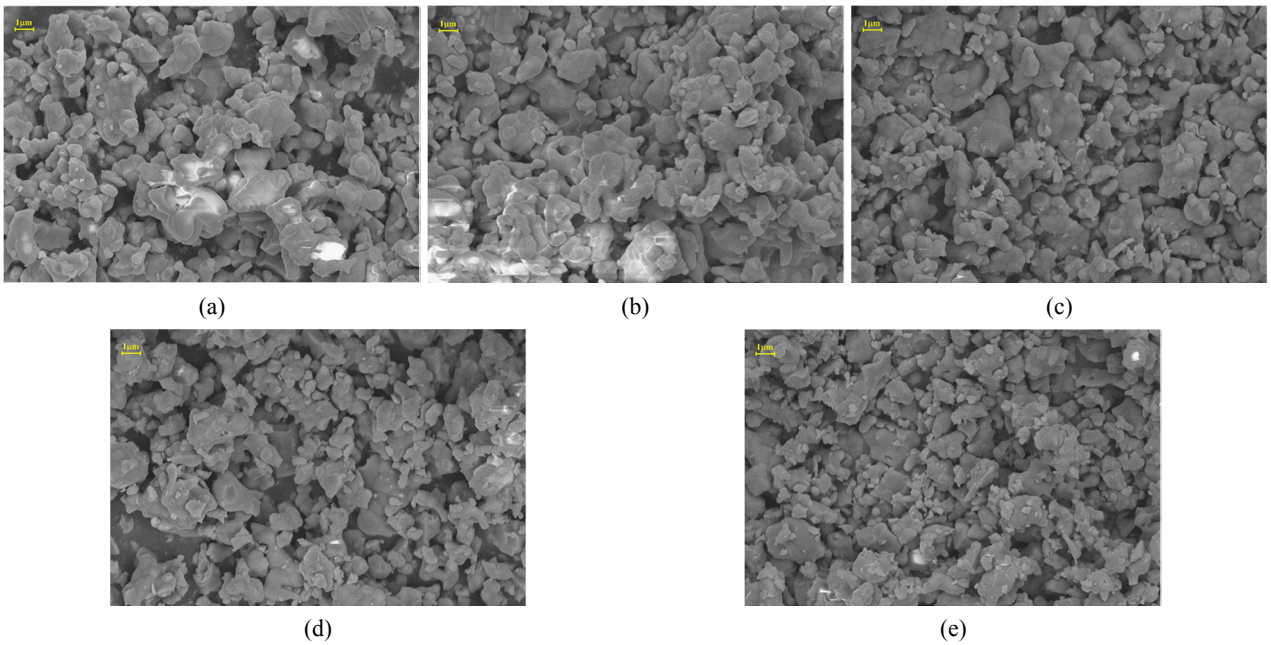

Fig.1. SEM photographs at 5K× magnifications of calcined powder after different ball milling times in (a) Sample A (0.5Hr), (b) Sample B (1.0Hr), (c) Sample C (1.5Hr), (d) Sample D (2.0Hr), and (e) Sample E (2.5Hr).

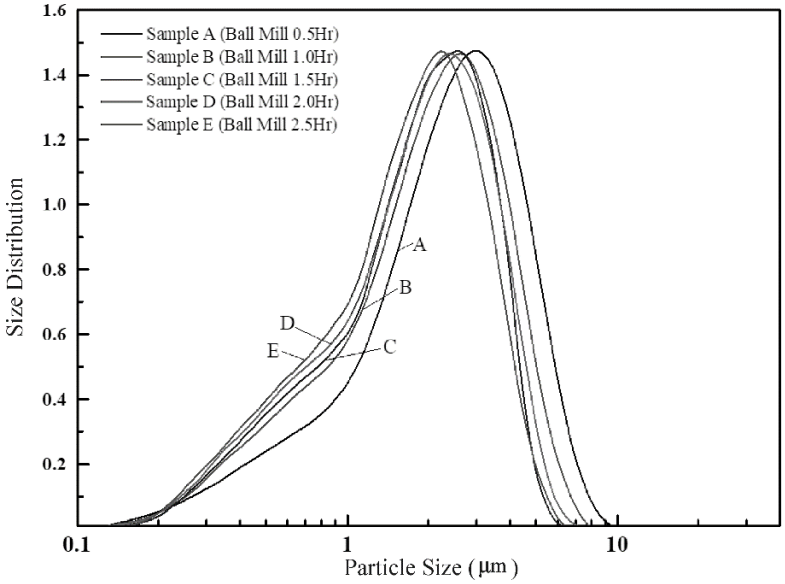

Fig.2. Comparison of particle size of the calcined powder of Samples A–E after different ball milling times.

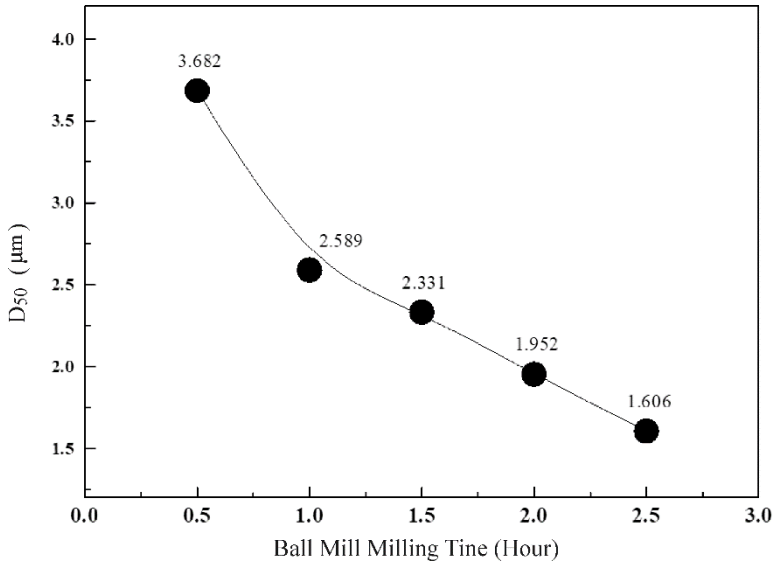

Fig.3. Data of average particle size (D_{50}) of the calcined powders after different ball milling times.

distribution is essential. The effects of different ball milling times on the particle size of the calcined powder of Samples A–E after different ball milling are also presented in Fig.2. A similar phenomenon has been observed in different samples after prolonged milling, with the narrowest particle size distribution obtained when using a longer ball milling time. The average particle size and distribution could be expected to be small and narrow for a starting powder, which is typically used in the ferrite-making industry and in a lot of studies on ferrites. To further investigate the magnetic properties of Mn and Al-doped YIG ferrites, the samples with different particle size after pressing were prepared and sintered at 1400°C. The surface morphology was also observed using SEM photographs at magnifications of 2K×, as shown in Fig.4, after the sample was polished using 0.03 μm Al_2O_3 powder and a hot corrosion process. Gold coating sample surfaces were used to yield SEM images of the microstructure. Microstructural measurements such as average grain size and their distributions were obtained using the aforementioned images. The size of the grains was obtained by taking at least 100 different crystallite grain samples and estimating the mean diameters of each individual grain. J-image software was used and calibrated with a scale bar during sample measurements. These figures demonstrated that as the ball milling time of the samples increased, the particle size decreased and thus the average grain size of the

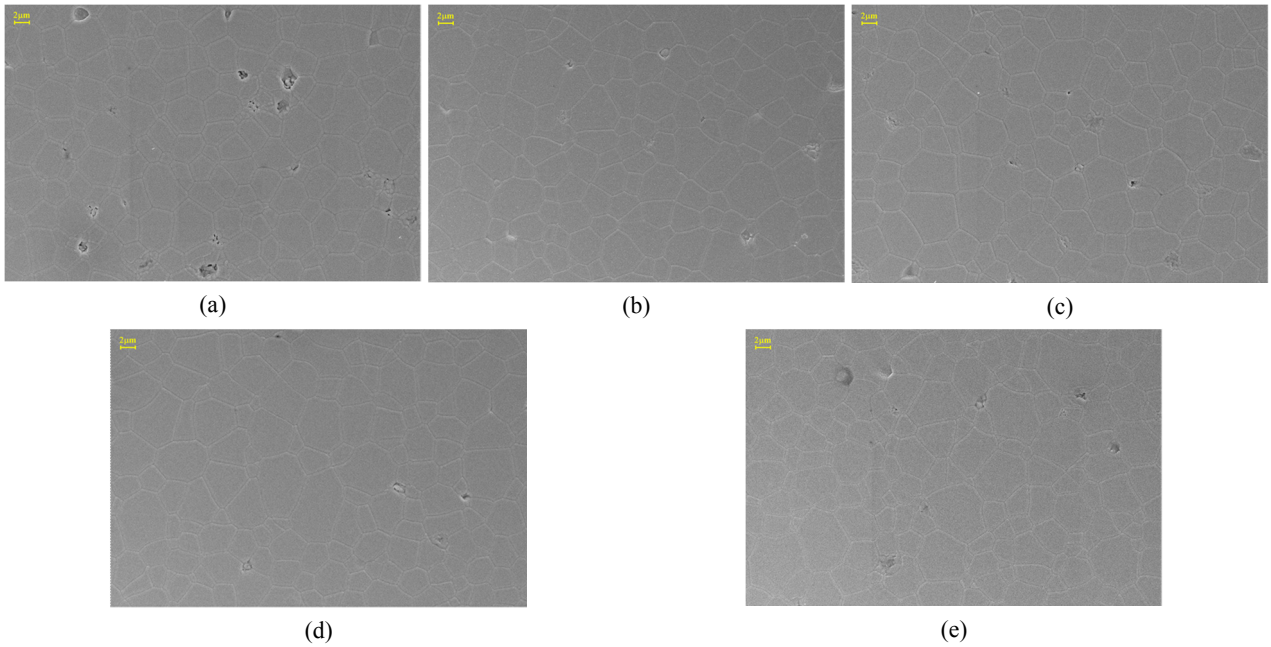

Fig.4. SEM photographs at 2K× magnifications of sintered specimens for different particle size in (a) Sample A, (b) Sample B, (c) Sample C, (d) Sample D, and (e) Sample E.

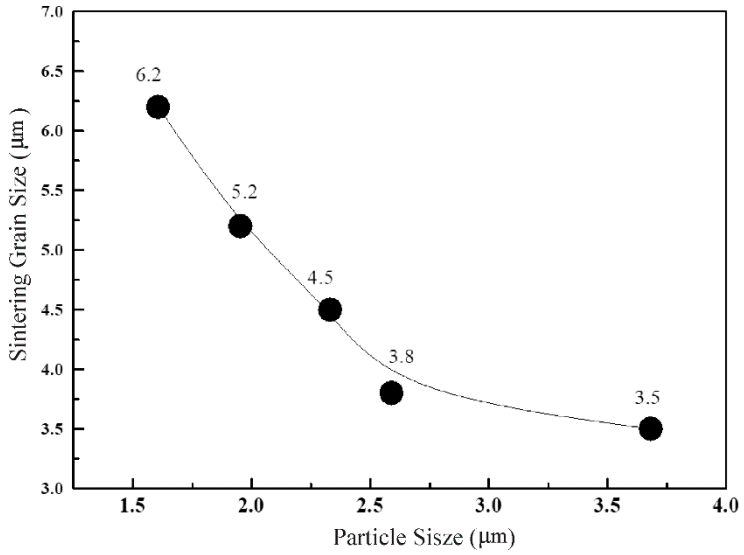

Fig.5. The grain size dependence on the particle size of the five sintered samples.

sintering crystallite increased. These results confirmed that the sintered grain exhibited a crystal size that increased from its initial values (average crystal grain sizes of 3.5 ± 0.1 μm for 0.5 h of milling) up to 6.2 ± 0.1 μm after ball milling for 2.5 h and in the subsequent sintering process.

Fig.7 presents the XRD patterns of the sintered samples with Mn and Al substitutions, which revealed the formation of $(Y_3)(Mn_{0.1}Al_{0.7}Fe_{4.2})\ O_{12}$ in different process conditions. Because the ionic radii of Mn^{2+} (0.067 nm) and Al^{3+} (0.0675 nm) are close to that of Fe^{3+} (0.064 nm), the incorporation of Mn^{2+} and Al^{3+} could not yield a variation in the lattice parameters. Thus, from the identified XRD patterns, a single-phase $(AlFe_4)Y_3O_{12}$ without extra phases, such as $YFeO_3$ and Fe_2O_3, was confirmed for all the samples by the Joint Committee in Powder Diffraction Standards reference code of 00-044-0228 regarding powder diffraction data, which indicated that crystalline YIG ($YFeO_3 + Fe_2O_3 \rightarrow Y_3Fe_5O_{12}$) was formed through ball milling at 1400°C sintering for 1 h[19].

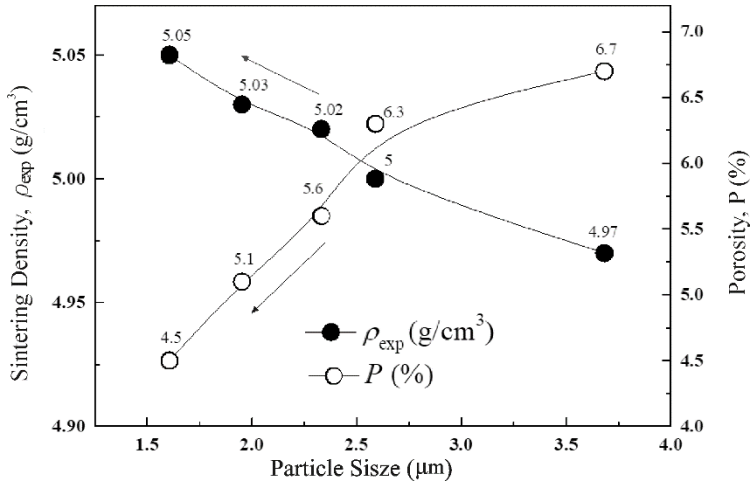

Fig.6. The density and porosity of the sintered samples as a function of particle size.

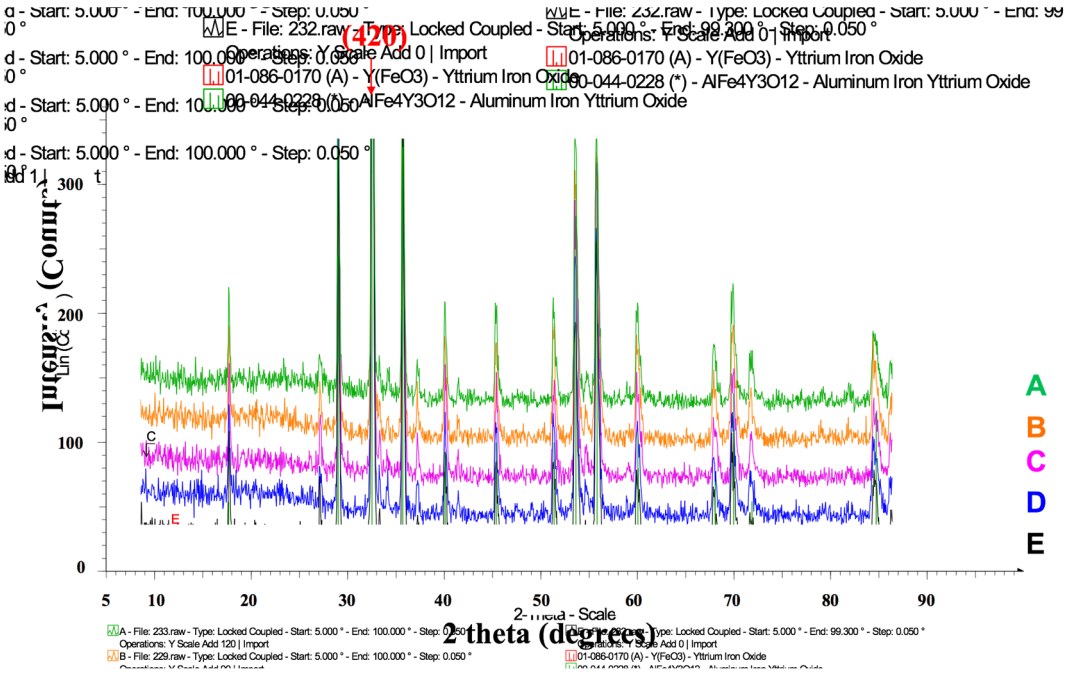

Fig.7. XRD patterns of the sintered samples for decreasing particle size with increasing ball milling times.

This information is crucial because ultimately, only the single phase of $(AlFe_4)Y_3O_{12}$ is required for the samples to achieve excellent magnetic properties. The $YFeO_3$ or Fe_2O_3 phase only has weak ferromagnetism and therefore does not contribute to such excellent properties. The XRD patterns in Fig.7 also demonstrated that the most intense peak (420) became narrower and sharper with decreasing the particle size, indicating the enhancement of crystallinity, and grain size, also in addition to the release of internal strains after sintering. From the reduction of internal strains during sintering, the enhancement of crystallinity, and the increase of crystallite grain size, magnetic domain walls move more easily, yielding higher magnetic permeability and magnetization of the sample. These changes are caused by calcined powder being milled for a prolonged time, and convert much of the amorphous phase associated with surfaces of nanometer-sized grains to the crystalline phase of the micron-sized grains. This phenomenon is due to higher reactivity between the finer as-milled calcined powders yielded by the prolonged ball milling time and decreased particle size.

Notably, a mass transport mechanism began with atomic surface diffusion and continued to occur through particle grain boundary diffusion, resulting in contact growth, pore elimination, and particle grain growth[19-20]. The evolution of a larger sintering grain size from a finer size of as-milled calcined powder through a prolonged ball milling time can be accompanied by the evolution of magnetic order from superparamagnetism to ferromagnetism. This description of microstructure evolution could be related to the results presented in Fig.5, where the curves of the grain size in the sintering samples corresponding to different particle size were plotted. This data indicated that in samples with prolonged milling times, the particle size decrease and subsequently an obvious increase of average grain size was achieved. The density of the sintering samples increased from 4.97 g/cm^3 to 5.05 g/cm^3, whereas the amount of porosity decreased from 6.7% to 4.5% with an decreased particle size, as shown in Fig.6, which suggests that all samples were adequately densified.

The amount of porosity, *P,* shown in Fig.6 is calculated by (1) as follows[20]:

$$P = \left(1 - \rho_{exp}/\rho_{xrd}\right) \times 100\% \quad (1)$$

where ρ_{exp} is experimental density determined from the Archimedes method and ρ_{xrd} is the X-ray density [21]. The X-ray density was calculated using (2) as follows [20]:

$$\rho_{xrd} = 8M/N_a a^3 \quad (2)$$

where ρ_{xrd} is the X-ray density, M is the molecular weight of a sample, N_a is the Avogadro's number, and a is the lattice constant that was calculated by indexing the XRD pattern. Paying more attention to the amount of porosity (*P)* is crucial for achieving fewer pinning centers in the movement of the domain walls, thus decreasing the demagnetizing effects in the sintering sample and enhancing its magnetic permeability[22]. Moreover, porosity is a cause of microwave loss. The results in Fig.6 should be viewed together with the larger sintering grain size distribution in Fig.4. These distributions appear to control the magnetic properties ($4\pi M_s$, B_r, *SQR*, H_c, ΔH), which is discussed in the next section.

3.2 Magnetic Properties

For a phase shifter design, an optimum YIG ferrite can be selected for a frequency with the following relationship[23]

$$\gamma 4\pi M_s/\omega \approx 0.6 \quad (3)$$

where © = 2.8 MHz/Oe is the gyromagnetic ratio of the ferrite and w is the operation frequency. For a 3.2 GHz application, a sufficient $4\pi M_s$ of less than 650 Gauss with an H_c of less than 1.0 Oe is desired. For YIG ferrites, the magnetic properties are strongly dependent on composition as well as on extrinsic properties, for example the microstructure of polycrystalline YIG after the sintering process. Therefore, the properties of hysteresis loop were first evaluated for Mn and Al-doped YIG ferrite samples with different particle size. Fig.8 illustrates how the ball milling time of the as-calcined powders affects the $4\pi M_s$, remanence (B_r), *SQR* (namely $B_r/4\pi M_s$), and H_c of the sintered YIG samples. As shown in Fig. 8, the samples exhibited a continual promotion of $4\pi M_s$ and B_r, and reduction in H_c with a decreased particle size. This trend was in agreement with the increase in crystallite grain size evidenced by the sintered samples depicted in Fig.4. These results explain the predominant size reduction effect on the as-milled calcined powders. As the calcined powder size decreases after ball milling, the crystallite grain size increases after sintering due to the higher reactivity between the finer as-milled calcined powders (larger SSA) yielded by the prolonged ball milling time. In the phase shifter, the *SQR* has a vital influence on signal switching. It has been noted that the Mn substitution of YIG is effective at increasing B_r due to its smaller magnetostriction constant ($\lfloor_{111}$)[11, 24]. The smaller the $\lfloor_{111}$, the higher B_r will be; thus, the *SQR* increases with the B_r. The stoichiometry of $(Y_3)(Mn_xAl_{0.8-x}Fe_{4.2})O_{12}$ with x = 0.1 used in this study was chosen in order to achieve a high *SQR*[11]. As shown in Fig.8, the *SQR* was upgraded because the increase in rates of $4\pi M_s$ and B_r were different. After 2.5 h of ball milling to obtain particle size=1.606⌈m, the H_c reached 0.948 Oe; concurrently, the $4\pi M_s$ and *SQR* of the five samples were also considerably affected by the milling process and varied in the 631–650 Gauss and 0.890–0.898 ranges, respectively, which met the specification requirements of commercial latch S-band phase shifter applications.

Regarding microwave materials, the losses were related to the absorption effect (degree of interaction) of microwaves in the materials, which mainly comprises electrical loss and magnetic loss. First, the electrical loss in material was related to the material's complex permittivity ε denoted by $\varepsilon = \varepsilon' - j\varepsilon''$, where the real part ε' is the relative dielectric constant and the imaginary part ε'' is the effective relative dielectric loss factor. The real part of the relative permittivity has also been denoted by $\varepsilon_r = \varepsilon'/\varepsilon_0$, where ε_0 is the permittivity of free space ($8.854 \oplus 10^{-12}$ F/m). When microwaves penetrate and propagate through a dielectric material, the internal field generated within the effected volume induces translational motions of free or bound charges, such as electrons or ions, and rotates charge complexes such as dipoles. Inertial, elastic, and frictional forces resist these

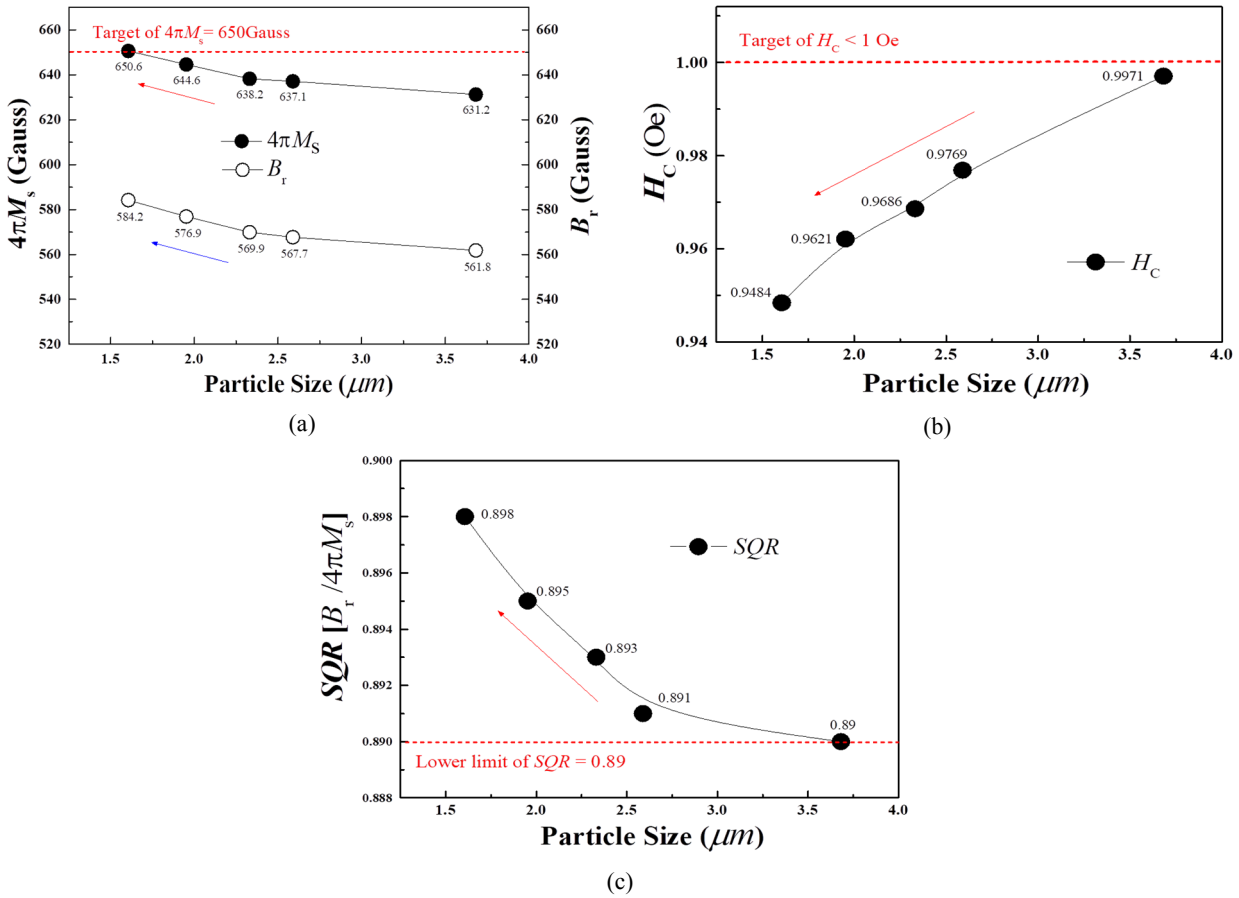

Fig.8. The particle size dependence of (a) the saturation magnetization, $4\pi M_s$, and the remanence, B_r, (b) the coercivity, H_C, and (c) the squareness of the magnetization loop, *SQR*.

induced motions and cause losses, a consequence of which is volumetric heating[25]. The loss tangent tanδ is commonly used to determine these losses, which is defined as tan™ $= \varepsilon'' / \varepsilon' = \sigma / 2\pi f \varepsilon_0 \varepsilon'$, where σ is the total effective conductivity (S/m) caused by ionic conduction and displacement currents and f is the frequency. The corresponding relative dielectric constant (ε_r) and dielectric loss (tanδ) for the samples with different particle size are shown in Fig.9. The samples exhibited a continual reduction in tanδ, and decreased particle size was associated with the enhancement of ε_r. These results may be related to the larger sintering grain size of YIG because the reduction of the as-milled calcined particle size created the more reactive surfaces of these powders.

The magnetic losses in materials affect the $|S_{21}|$ of the microwave device, which is related to the imaginary part of the permeability of the positive polarization μ'', which increases with the FMR line width, that is, ΔH. Because the $(Y_3)(Mn_{0.1}Al_{0.7}Fe_{4.2})O_{12}$ ferrites sintered at 1400°C showed optimum magnetic properties, the critical parameter of microwave magnetic material concerning the magnetic losses, ΔH, was also measured at 3 dB of the absorption peak in accordance with ASTM A883/A883M-01. In this study, ΔH was measured at a frequency of 3.2 GHz using a nondestructive FMR spectrometer, based on the local excitation of magnetostatic wave resonance in a small area of the film under a bias magnetic field with a hole-like profile. The FMR curve and ΔH trend for the five samples with different particle size of the $(Y_3)(Mn_{0.1}Al_{0.7}Fe_{4.2})O_{12}$ ferrites are illustrated in Fig.10 (a) and (b), respectively. The size reduction effect of the as-milled calcined powder that contributed to the larger sintering grain size could explain the aforementioned results. The Mn and Al-doped YIG ferrite experienced a 47% decline in the 3 dB line width of ΔH, which was predominantly attributed to the sintering grain size increasing from 3.5 ± 0.1 μm at the beginning to 6.2 ± 0.1 μm at the end of the 2.5-h ball milling (particle size=1.606⌈m) and subsequent sintering. This phenomenon is also consistent with the results of Figs.1–4, which match the variation in the other magnetic properties ($4\pi M_s$, B_r, *SQR*, H_c). The narrowest ΔH, determined to be 22.9 Oe at 3.2 GHz for Sample E, was still sufficiently low for device purposes. The $|S_{21}|$ can be considered to be almost the same as the magnitudes of S-parameter S_{21}. Regarding the Mn and Al-doped YIG

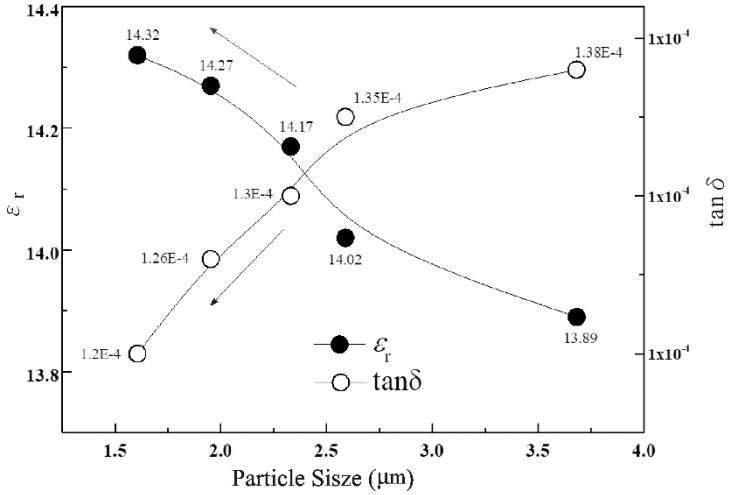

Fig.9. The particle size dependence of the relative dielectric constant, ε_r, and loss tangent, tanδ.

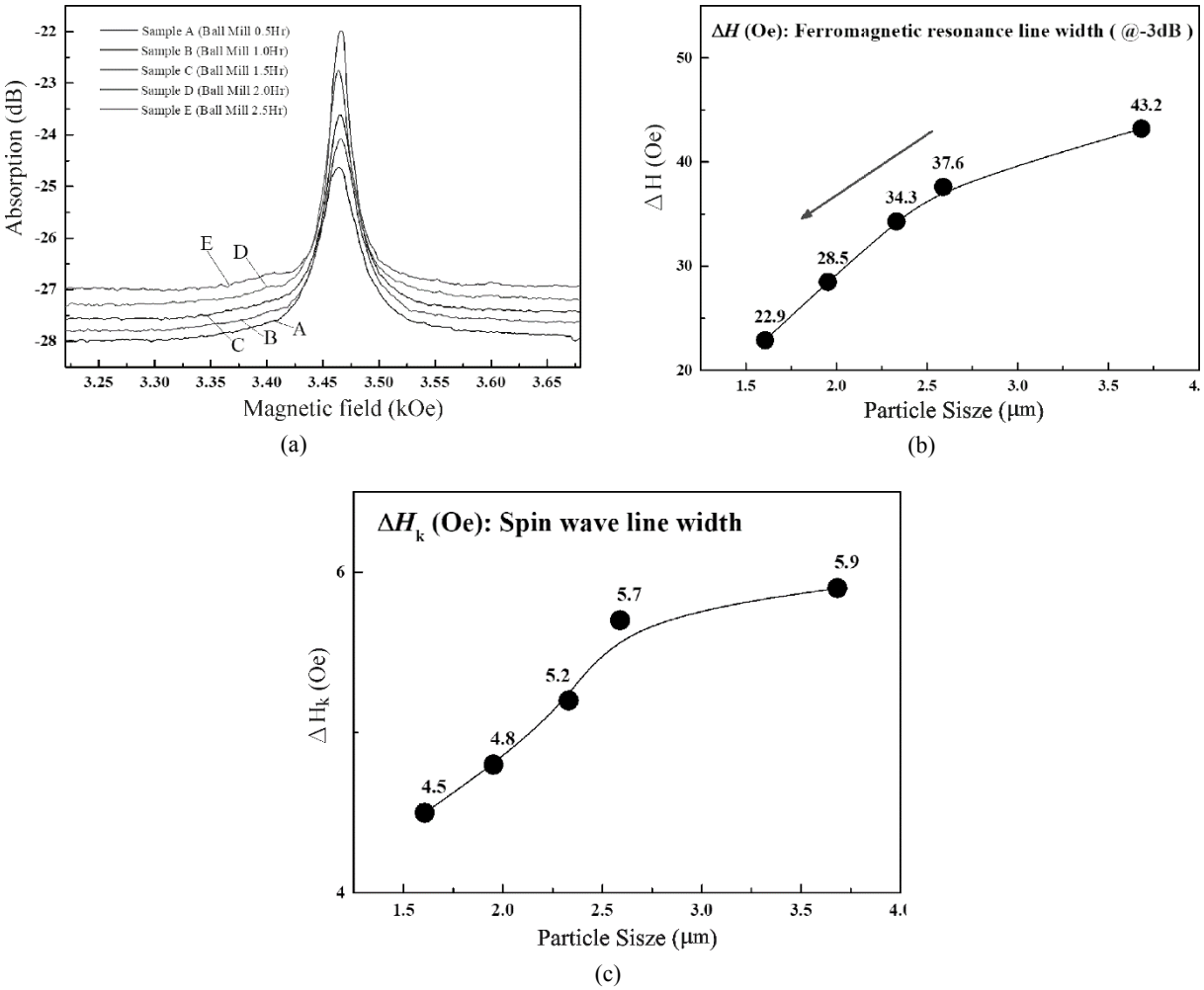

Fig.10. The particle size dependence of (a) the ferromagnetic resonance curve, (b) ΔH, and (c) ΔH_k.

ferrite of Sample E that was modularized in the latching-type phase shifter, $|S_{21}|$ was evaluated using an Agilent E5071B vector network analyzer at 3.2 GHz to be 0.9 dB, a value sufficiently low to meet the requirement of

this microwave device.

For YIG ferrite material applied in microwave devices above a certain microwave power level, nonlinear phenomena lead to additional magnetic loss, which rapidly becomes prohibitive in the devices. The nonlinear effects are associated with the excitation of the spin waves, the attenuation of which can be clarified through ΔH_k. Such nonlinear effects occur in the ferrite while the applied static field exceeds the critical magnetic microwave field h_{crit}. The value of ΔH_k was extracted from the spin-wave instability threshold field h_{crit}, with a specific relation as indicated in[26]:

$$h_{crit} = 2f\Delta H_k/\gamma M_s \quad (4)$$

The higher the value of ΔH_k in the YIG ferrite material, the greater the power handling capability of the microwave devices. Regarding the five samples with different ball milling times of the Mn and Al-doped YIG ferrites in this research, their ΔH_k decreased from 5.9 Oe to 3.5 Oe after 2.5 h of ball milling, which was a reverse trend to ΔH. This drop in ΔH_k was mainly attributed to the smaller particle size and subsequent sintering. Small grains, however, are superior to large grains for high-power operations. This is because small grains produce a larger ΔH_k due to transit time limitations[26]. The ΔH_k was determined to be 3.5 Oe at 3.2 GHz for Sample E, which is still sufficiently low for low-loss phase shifters and circulator applications[26].

A careful analysis of corresponding properties for the as-milled calcined particle sizes and sintering crystal sizes in Table 1 exhibited a correlation with prolonged ball milling time and decreasing particle size.

4. CONCLUSIONS

The strong dependence of the microstructure and magnetic properties of single-phase Mn and Al-doped YIG ferrites on ball milling times and related particle size becomes evident at the microscale. After prolonged ball milling, as-milled calcined powders exhibited a particle size reduction from D_{50} = 3.682 μm to 1.606 μm. Tailoring of magnetic properties was realized due to the prevalence of different influences when sintered crystal sizes are changed. The sintering crystal size increased from 3.5 ± 0.1 μm to 6.2 ± 0.1 μm after 2.5 h of ball milling and the subsequent sintering process was attributed to faster and higher reactivity between the finer as-milled calcined powders yielded by the prolonged ball milling time, as indicated from the analysis of the corresponding SEM and more intense (420) peak of the XRD pattern. Regarding Sample E, its $4\pi M_s$ increased from 631 to 650 Gauss, B_r increased from 562 to 584 Gauss, and *SQR* increased from 0.890 to 0.898, whereas H_c decreased from 0.997 to 0.948, tanδ decreased from 1.38×10^{-4} to 1.20×10^{-4}, and ΔH decreased from 43.2 to 22.9 Oe after 2.5 h of ball milling for 1.606⌈m particle size and the subsequent sintering process. For Sample E, which underwent 2.5 h of ball milling, ΔH_k was determined to be 3.5 Oe, whereas the insertion loss regarding the Mn and Al-doped YIG ferrite modularized in the latching-type phase shifter described by $|S_{21}|$ was evaluated to be 0.9 dB. These were both confirmed to be sufficiently low for low-loss microwave devices applications. A connection between the changes of sample microstructures as a function of particle size and corresponding magnetic properties was made. However, the intricate effects of each variable on the intrinsic and extrinsic properties could be further explored regarding Mn and Al-doped YIG ferrites exhibiting an enhanced ferromagnetic phenomenon, and the contributions thereof to magnetic properties. From our study, the same principles could be extended to ferrite process applied in a wide range of low-frequency microwave devices if an appropriate process condition and the composition of the ferrite materials were selected.

Table 1 Summary of physical and magnetic properties with the relevant ball milling times and particle size.

Process Conditions			Physical Properties			Magneto-Electric properties							
Samples	Milling Time (Hr)	As-milled Calcined Powder Size, D_{50} (μm)	Sintering Crystal Size (μm)	Sintering Density, ρ_{exp} (g/cm^3)	Porosity (%)	$4\pi M_s$ (G)	B_r (G)	*SQR*	H_c (Oe)	ε_r	tanδ ($\times 10^{-4}$)	ΔH (Oe)	ΔH_k (Oe)
A	0.5	3.68	3.5	4.97	6.7	631	562	0.890	0.997	13.89	1.38	43.2	5.9
B	1.0	2.59	3.8	5.00	6.3	637	568	0.891	0.977	14.02	1.35	37.6	5.7
C	1.5	2.33	4.5	5.02	5.6	638	570	0.893	0.969	14.17	1.30	34.3	5.2
D	2.0	1.95	5.2	5.03	5.1	645	577	0.895	0.961	14.27	1.26	28.5	4.8
E	2.5	1.60	6.2	5.05	4.5	651	584	0.898	0.948	14.32	1.2	22.9	4.5

ACKNOWLEDGES

The authors would like to thank Mr. Hsin-Ming Hsu who contributed to the sample preparation and offered suggestions on the experiments. Special thanks also go to Mr. Chun-Jen Su, Mr. Jung-Yuan Hsieh and Mr. Sung-Jau Tsai for their support, as this work could not have been completed without them.

REFERENCE

1. Harris VG, Geiler A, Chen YJ, et al. Recent advances in processing and applications of microwave ferrites. J. Magn. Magn. Mater. 2009; 321:2035-2047.
2. Aldbea FW, Ibrahim NB, Yahya M. Effect of adding aluminum ion on the structural, optical, electrical and magnetic properties of terbium doped yttrium iron garnet nanoparticles films prepared by sol-gel method. Appl. Surf. Sci. 2014; 321:150-7.
3. Pardavi-Horvath M. Microwave applications of soft ferrites. J. Magn. Magn. Mater. 2000; 215:171-183.
4. Huang CC, Zuo WZ, Hung YH, Huang JY, Kuo MF, Cheng CH, et al. Effect of specific surface area of raw material Fe_2O_3 on magnetic properties of YIG. J. Magn. Magn. Mater. 2018; 449:157-164.
5. Yang H, Zhang G, Lin Y, Ye T, Kang P. Electrical, magnetic and magneticproperties of $BaTiO_3$/$BiY_2Fe_5O_{12}$ particulate composites. Ceram. Int. 2015; 41(5):7227-7232.
6. Harris VG, Geiler A, Chen Y, Yoon SD, Wu M, Yang A, et al. Recent advances in processing and applications of microwave ferrites. J. Magn. Magn. Mater. 2009; 321(14):2035-2047.
7. Ridrigue GP. Magnetism in Microwave Devices. J. Appl. Phys. 1969; 40:929-938.
8. Motlagh Z, Mozaffari M, Amighian J. Preparation of nano-sized Al-substituted yttrium iron garnets by the mechanochemical method and investigation of their magnetic properties. J. Magn. Magn. Mater. 2009; 321(13): 1980-1984.
9. Gilleo MA, Geller S. Magnetic and Crystallographic Properties of Substituted Yttrium-Iron Garnet, $3Y_2O_3{\cdot}xM_2O_3{\cdot}(5\text{-}x)Fe_2O_3$. Phys. Rev. 1958; 110:73-78.
10. Sharma P, Thakur P, Mattei JL, Queffelec P, Thakur A. Synthesis, structural, optical, electrical and Mössbauer spectroscopic studies of Co substituted $Li_{0.5}Fe_{2.5}O_4$. J. Magn. Magn. Mater. 2016; 407:17-23.
11. Huang CC, Hung YH, Huang JY, et al. Impact of Stoichiometry and Sintering Temperature to Magnetic Properties of $Y_3Mn_xAl_{0.83\text{-}x}Fe_{4.17}O_{12}$ Ferrites. IEEE Trans. Magn. 2014; 50: 2801004.
12. Adam JD, Davis LE, Dionne GF, et al. Ferrite Devices and Materials. IEEE Trans. Microwave Theory Tech. 2002; 50:721-736.
13. Paiva DVM, Silva MAS, Ribeiro TS, Vasconcelos IF, Sombra ASB, Góes JC, et al. Novel magnetic–dielectric composite ceramic obtained from $Y_3Fe_5O_{12}$ and $CaTiO_3$. J. Alloy. Compd. 2015; 644:763-769.
14. Musa MA, Azis RS, Osman NH, Hassan J, Zangina A. Structural and magnetic properties of yttrium iron garnet (YIG) and yttrium aluminum iron garnet (YAlG) nanoferrite via sol-gel synthesis. Results in Physics. 2017; 7:1135-1142.
15. Chou HM, Case ED. Characterization of some mechanical properties of yttrium iron garnet (YIG) by non-destructive method. J. Mater. Sci. Lett. 1988; 7:1217-1220.
16. International standard IEC 60556, https://webstore.iec.ch/publication/2500&preview=1.
17. Hakki BW, Coleman PD. A dielectric resonator method of measuring inductive capacities in the millimeter range. IEEE Trans. Microwave Theory & Tech. 1960; 8:402-410.
18. Kobayashi Y, Katoh N. Microwave Measurement of Dielectric Properties of Low-loss Materials by the Dielectric Rod Resonator Method. IEEE Trans. Microwave Theory & Tech. 1985; 33:586-592.
19. Sztaniszláv A, Sterk E, Fetter L, et al. Investigation of garnet formation by sintering of Y_2O_3 and Fe_2O_3. J. Magn. Magn. Mater. 1984; 41:75-78.
20. Rodziaha N, Hashima M, Idza IR, Ismayadi I, Hapishah AN, Khamirul MA. Dependence of developing magnetic hysteresis characteristics on stages of evolving microstructure in polycrystalline yttrium iron garnet. Appl. Surf. Sci. 2012;258: 2679- 2685.
21. Shinde TJ, Gadkari AB, Vasambekar PN. DC resistivity of Ni-Zn ferrites prepared by oxalate precipitation method. Mater. Chem. Phys. 2008; 111:87-91.
22. Naughton BT, Majewski P, Clarke DR. Magnetic properties of nickel-zinc ferrite toroids prepared from nanoparticles. J. Am. Ceram. Soc. 2007; 90(11): 3547–3553.
23. Hord WE. Design Considerations for Rotary-Field Ferrite Phase Shifters. Microwave J. 1988; 31:105-115.
24. Dionne GF, Paul PJ, West RG, et al. Compensation of Magnetostriction Effects in Iron Garnets by Manganese Additions. J. Appl. Phys. 1970; 41:1411.
25. Sutton WH. Microwave Processing of Ceramic Materials. Am. Ceram. Soc. Bull. 1989;68(2):376-386.
26. Patton CE. Ferrite Materials for Advanced Multifunction Microwave Systems Applications. Final Report to the United States Office of Naval Research; October 1, 2002 - March 31, 2006; ONR N00014-03-1-0070. □